3B2v8.06a/w (Dec 5 2003).51c XML:ver:5.0.1 NIMA : 43722 Prod.Type:COM pp.1–18(col.fig.:NIL) ED:M.S.Usha PAGN:mamatha SCAN:venugopal

Available online at www.sciencedirect.com

SCIENCE DIRECT®

ELSEVIER

Nuclear Instruments and Methods in Physics Research A ▮ (▮▮▮▮) ▮▮▮–▮▮▮

NUCLEAR INSTRUMENTS & METHODS IN PHYSICS RESEARCH Section A

www.elsevier.com/locate/nima

Electrical characterization of large volume CdZnTe coplanar detectors

R. González[a], J.M. Pérez[a,*], O. Vela[a], E. de Burgos[a], J.C. Oller[a], V. Gostilo[b]

[a]*Laboratorio General de Electrónica y Automática, CIEMAT, Edificio 22, Avenida Complutense, 22, E-28040 Madrid, Spain*

[b]*BSI, Ltd., Ganibu Dambis 26, P.O. Box 33, Riga LV-1005, Latvia*

Received 8 November 2004; received in revised form 14 February 2005; accepted 11 March 2005

Abstract

The electrical behaviors of two large volume CZT coplanar detectors in the voltage and temperature application range are presented in this work. Two different regions are treated: bulk and anode surface. $I-V$ curves were acquired at different temperatures in these two regions. Experimental results were analyzed by treating the device as a metal–semiconductor Schottky barrier. Two different formulations were used for modeling this structure: the interfacial-layer thermionic-diffusion model, considered as a complete and general theory, and the diffusion model as a more specific approach. It will be shown that the diffusion model is sufficient to reproduce the results obtained for biases and temperatures normally used in operation. A detailed description of this model is provided. In the anode face, the diffusion model is compared with the space-charge-limited current theory. Differences found in the two regions studied are outlined in this paper. Finally, the influence of the electrical parameters in the design of future detectors is discussed.

PACS: 29.40.Wk; 72.80.Ey; 73.40.Rw; 73.40.Sx

Keywords: CdZnTe; CZT; Gamma detectors; Coplanar; ITD; Diffusion model; Electrical current

1. Introduction

Recent works [1–3] have demonstrated that CZT detectors with volume larger than 2 cm^3 and energy resolution in the order of 2.5% FWHM for ^{137}Cs can be realistic options for practical applications. In the development of large volume detectors, additional difficulties arise, compared with the ones having conventional dimensions. First, homogeneity in electrical properties affecting carrier transport and trap densities is much more difficult to obtain. Second, correct surface preparation and electrode deposition are

*Corresponding author. Tel.: +34 91 346 6557; fax: +34 91 346 6275.
E-mail address: jm.perez@ciemat.es (J.M. Pérez).

0168-9002/$ - see front matter © 2005 Published by Elsevier B.V.
doi:10.1016/j.nima.2005.03.147

especially important, since non-conventional electrodes such as coplanar anodes or pixel arrays are needed in such thick detectors for high-resolution spectrometry. Gaps between strips in coplanar electrodes are so narrow that only a very good quality surface enables a correct electric field distribution in the surface.

As a consequence of the above observations, large volume CZT devices are more sensitive to surface and bulk problems than conventional devices. A good knowledge of their electrical properties is therefore a major issue. The aim of this paper is to report current measurements performed on two large volume CZT coplanar detectors with gold electrodes and the interpretation of the experimental data according to theoretical models. One of the detectors, labeled as M02.2-1, was constructed by eV-Products, USA, with dimensions 1.5 cm diameter and 1.0 cm thick. It is a coplanar grid detector, with anode pattern corresponding to generation *IV* design with cylindrical symmetry reported elsewhere [4]. The CdZnTe crystal of the second unit, referred in this work as M0904, was grown and processed by eV-Products. Electrode deposition and detector mounting were carried out by BSI, Latvia. The dimensions of the detector were $1.5\,\mathrm{cm} \times 1.5\,\mathrm{cm}$ area and 1.0 cm thick. The same coplanar grid design was used for this detector, this time using the generation *IV* pattern with rectangular symmetry [5].

The main goal of the measurements presented in this paper is the characterization of the detectors as electrical devices in their operation range. Since these units were developed to be used as sensors in remote radiation survey systems, we will mainly concentrate on the voltage and temperature ranges of interest to their practical application. Operation bias for the cathode in these detectors is between 1000 and 1800 V, whereas a differential bias on the order of 20 V must be applied between anodes for the coplanar detector to work in the differential anode gain mode [6]. Nominal operation temperature range will be between 10 and 50 °C.

CZT detectors are modeled as metal–semiconductor–metal devices with two back-to-back Schottky barriers. Several treatments were applied to this model within the last few years. From our point view, the interfacial-layer thermionic-diffusion (ITD) model is the one that better fits the experimental results with a detector similar to the ones reported in this paper. This model, together with the diffusion model, is used in this work to interpret the $I-V$ curves. A detailed presentation of the second model is provided. A discussion concerning the applicability of this model to our detectors is also presented in this paper. Two different regions are treated: the bulk, currents between anodes and cathode, and anode surface, currents between collecting anode and non-collecting anode. Finally, the influence of this electrical characterization in the design of future detectors is discussed.

2. Models for carrier transport in CZT devices

2.1. Transport theories in Schottky barriers

The two basic theories for modeling the majority-carrier transport through a Schottky barrier fabricated on lightly doped semiconductors are the thermionic emission theory and the diffusion theory. Both theories are based on the assumption that the barrier height is much larger than kT [7]. The thermionic theory also assumes that the carrier collision in the depletion layer of the semiconductor is negligible. In the diffusion model, the carrier transport across the barrier height is mainly limited by carrier diffusion in the space-charge region of the semiconductor. Comparing these two models, the thermionic theory is more likely to be valid for semiconductors in which the doping level is expected to give a free carrier concentration in excess of about $10^{14}\,\mathrm{cm}^{-3}$ and where the application of modest biases can produce carrier avalanching or minority carrier injections [8]. For thick detectors with relatively low mobility and high resistivity, such as the ones reported in this work, the diffusion model is expected to be a better approach.

However, the two theories above did not satisfactorily interpret the $I-V$ characteristics measured in the Schottky barrier diodes in all the cases. A more general theory based on the assumption that an interfacial layer of atomic dimension was created between the metal and the semiconductor was developed in order to consider the origin of the barrier height formation. This new theory, based on the interfacial-layer concept, included the effects of the applied bias drop and a transmission coefficient across the interfacial layer [9]. A synthesis theory for majority-carrier transport was developed by Wu [10], which incorporated the thermionic emission theory, diffusion theory and interfacial-layer theory into the so-called ITD theory.

Bolotnikov et al. [11,12] validated this model for CZT devices. According to their experimental results, the thermionic-diffusion model only reproduced the measured currents at low voltages. At high voltages, the measured curves increased much faster than the predicted curves by this theory. The inclusion of the insulating layer predicted by the ITD model enabled experimental and theoretical results to fit very accurately. The presence of the interfacial layer causes the current to decrease significantly at low biases and to rise exponentially at very high bias. A detailed formulation of the dependence of current density versus applied voltage can be found in Ref. [10]. A more practical formulation to fit experimental data with CZT detectors is given in Ref. [11] which according to the author's opinion, is one of the most rigorous works published on this subject for CZT detectors.

In this paper, we show that the ITD theory can be excessively complex for interpreting our detectors. We compare the results of the ITD theory and the diffusion model. The application of the diffusion model to devices similar to the ones presented in this paper is not widely reported in the literature. To better understand the fits we obtain, a detailed formulation of the diffusion model is provided.

2.2. Diffusion model

The formulation of the diffusion model in our devices is outlined below, and was derived basically from the treatment of the diffusion model in Refs. [7,8]. An important simplification can be made in the two back-to-back Schottky barrier formulations for our metal–semiconductor–metal devices. Because of the high resistivity of this material, the series resistance of the undepleted bulk material is much higher than the resistance of the forward-biased Schottky barrier,

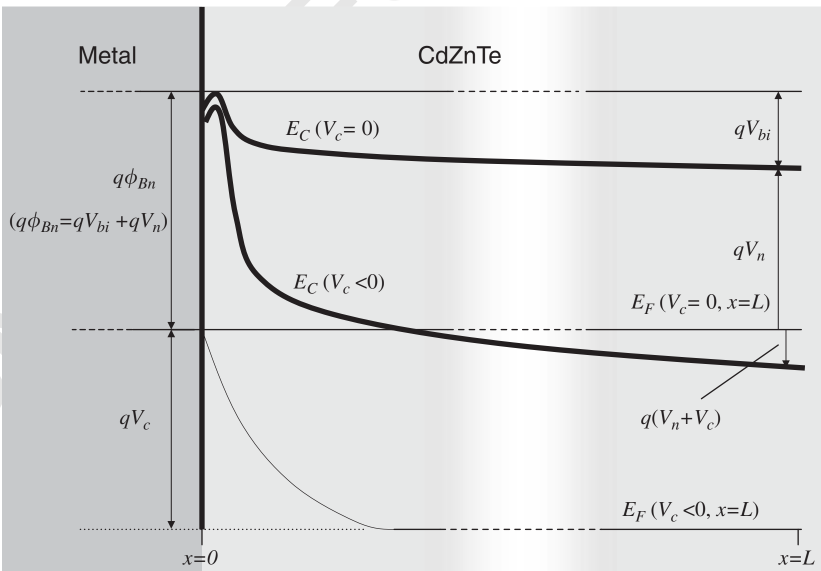

Fig. 1. Energy band diagram proposed for the CdZnTe–metal contact.

and the width of the depleted barrier in this contact is much smaller than the detector thickness. Therefore, the effect of this barrier can be disregarded and the CZT detector can be considered as a reverse biased Schottky metal–semiconductor (or semi-insulating) contact. The energy band diagram of this contact is represented in Fig. 1, at two different biases: $V_c = 0$ and reverse bias ($V_c < 0$) assuming thermal equilibrium. E_c represents the conduction band and E_F the Fermi level. ϕ_{Bn} is the barrier height at thermal equilibrium, V_{bi} the built-in potential and $V_n = \phi_{Bn} - V_{bi}$ [7].

In the space-charge region of this contact, the carrier transport is generally described by the conventional current flow equation. Assuming a one-dimensional (1D) n-type semiconductor device, this equation is given by

$$\begin{aligned} j &= (-q)\left[n(x)\mu_n E(x) + D_n \frac{\partial n(x)}{\partial x}\right] \\ &= (-q)D_n\left[-\frac{q}{kT} n(x)\frac{\partial V(x)}{\partial x} + \frac{\partial n(x)}{\partial x}\right] \end{aligned} \tag{1}$$

where q is the electron charge, $n(x)$ the free carrier concentration, μ_n the carrier mobility, D_n the diffusion coefficient, k the Boltzmann's constant, T the temperature and $E(x)$ and $V(x)$ the electric field and voltage within the semiconductor, respectively.

By using $e^{-(q/kT)V(x)}$ as integration factor,

$$\begin{aligned} j e^{-(q/kT)V(x)} = (-q)D_n\bigg[&-\frac{q}{kT} n(x)\frac{\partial V(x)}{\partial x} e^{-(q/kT)V(x)} \\ &+ \frac{\partial n(x)}{\partial x} e^{-(q/kT)V(x)}\bigg]. \end{aligned} \tag{2}$$

Integrating both sides of the equation from $x = 0$ to $x = L$, with L being the detector thickness,

$$\begin{aligned} &\int_0^L j e^{-(q/kT)V(x)}\,dx \\ &= (-q)D_n\left[\int_0^L n(x)\frac{\partial}{\partial x} e^{-(q/kT)V(x)}\,dx \right. \\ &\quad \left. + \int_0^L \frac{\partial n(x)}{\partial x} e^{-(q/kT)V(x)}\,dx\right] \\ &= (-q)D_n \int_0^L \frac{\partial}{\partial x}\left(n(x)\,e^{-(q/kT)V(x)}\right) dx. \end{aligned} \tag{3}$$

Therefore,

$$\int_0^L j\, e^{-(q/kT)V(x)}\,dx = (-q)D_n\left[n(x)\,e^{-(q/kT)V(x)}\right]_0^L. \tag{4}$$

Since the current density is constant throughout the crystal under the steady-state condition

$$j\int_0^L e^{-(q/kT)V(x)}\,dx = (-q)D_n\left[n(x)\,e^{-(q/kT)V(x)}\right]_0^L \tag{5}$$

and j is given by the expression

$$j = (-q)D_n\left[n(x)\,e^{-(q/kT)V(x)}\right]_0^L \frac{1}{\int_0^L e^{-(q/kT)V(x)}\,dx}. \tag{6}$$

Considering the diagram in Fig. 1, the boundary conditions of the system are:

$$qV(x=0) = -q\phi_{Bn} \tag{7}$$

$$qV(x=L) = (-q)(V_n + V_c) \tag{8}$$

$$\begin{aligned} n(x=0) &= N_c\, e^{-(E_c(x=0) - E_F(x=0))/kT} \\ &= N_c\, e^{-(q/kT)\phi_{Bn}} \end{aligned} \tag{9}$$

$$\begin{aligned} n(x=L) &= N_c\, e^{-(E_c(x=L) - E_F(x=L))/kT} \\ &= N_c\, e^{-(q/kT)V_n} \end{aligned} \tag{10}$$

where N_c is the effective density of states in the conduction band. By substituting the expressions provided by the boundary conditions, we obtain

$$\begin{aligned} &-qD_n\left[n(x)\,e^{-(q/kT)V(x)}\right]_0^L \\ &= -qD_n\Big[N_c\, e^{-(q/kT)V_n}\, e^{-(-q/kT)V_n}\, e^{-(-q/kT)V_c} \\ &\quad - N_c\, e^{-(q/kT)\phi_{Bn}}\, e^{-(q/kT)(-\phi_{Bn})}\Big] \\ &= qD_n N_c\left[1 - e^{(q/kT)V_c}\right] \end{aligned} \tag{11}$$

and Eq. (6) becomes

$$j = qD_n N_c\left[1 - e^{(q/kT)V_c}\right]\frac{1}{\int_0^L e^{-(q/kT)V(x)}\,dx}. \tag{12}$$

Poisson's equation for a semiconductor with all its donor centers ionized, with a concentration of donor centers given by N_D, provides the approximate expression

$$\frac{\partial^2 V}{\partial x^2} \approx -\frac{qN_{\mathrm{D}}}{\varepsilon} \tag{13}$$

(provided that $n(x) \ll N_{\mathrm{D}}$ in the bulk). ε is the electrical permittivity in the crystal. Solving this elemental differential equation

$$V(x) = -\frac{qN_{\mathrm{D}}}{\varepsilon}\frac{x^2}{2} + C_1 x + C_2. \tag{14}$$

Applying boundary conditions (7) and (8):

$$qV(0) = -q\phi_{\mathrm{B}n} = qC_2 \Rightarrow C_2 = -\phi_{\mathrm{B}n} \tag{15}$$

$$\begin{aligned} qV(L) &= -q(V_c + V_n) \\ &= -q\frac{qN_{\mathrm{D}}}{\varepsilon}\frac{L^2}{2} + qC_1 L - q\phi_{\mathrm{B}n}. \end{aligned} \tag{16}$$

From Eq. (16),

$$\begin{aligned} C_1 L &= -(V_c + V_n - \phi_{\mathrm{B}n}) + \frac{qN_{\mathrm{D}}}{\varepsilon}\frac{L^2}{2} \\ &= -(V_c - V_{\mathrm{bi}}) + \frac{qN_{\mathrm{D}}}{\varepsilon}\frac{L^2}{2} \Rightarrow \\ C_1 &= \frac{-(V_c - V_{\mathrm{bi}})}{L} + \frac{qN_{\mathrm{D}}}{\varepsilon}\frac{L}{2}. \end{aligned} \tag{17}$$

Substituting in Eq. (14),

$$\begin{aligned} V(x) = \frac{qN_{\mathrm{D}}}{\varepsilon}\left[\left(\frac{\varepsilon}{qN_{\mathrm{D}}L}(-V_c + V_{\mathrm{bi}}) \right.\right. \\ \left.\left. + \frac{L}{2}\right)x - \frac{x^2}{2}\right] - \phi_{\mathrm{B}n}. \end{aligned} \tag{18}$$

If we define L_{D} and d as

$$\begin{aligned} L_{\mathrm{D}} &= \sqrt{\frac{\varepsilon}{qN_{\mathrm{D}}}\frac{kT}{q}} \\ d &= \frac{\varepsilon}{qN_{\mathrm{D}}L}(-V_c + V_{\mathrm{bi}}) + \frac{L}{2} \end{aligned} \tag{19}$$

the integral in the denominator for the expression of j in Eq. (12) can be expressed as

$$\begin{aligned} \int_0^L \mathrm{e}^{-(q/kT)V(x)}\,\mathrm{d}x &= \int_0^L \mathrm{e}^{-(q/kT)qN_{\mathrm{D}}/\varepsilon(dx-(x^2/2))} \\ &\quad \times \mathrm{e}^{(q/kT)\phi_{\mathrm{B}n}}\,\mathrm{d}x \\ &= \mathrm{e}^{(q/kT)\phi_{\mathrm{B}n}} \int_0^L \mathrm{e}^{((x^2/2)-dx)/L_{\mathrm{D}}^2}\,\mathrm{d}x. \end{aligned} \tag{20}$$

The integral in the last term of Eq. (20) will be evaluated in the following way. If we denote $t = x/L_{\mathrm{D}}$ and, $d' = d/L_{\mathrm{D}}$,

$$\begin{aligned} \int_0^L \mathrm{e}^{((x^2/2)-dx)/L_{\mathrm{D}}^2}\,\mathrm{d}x &= L_{\mathrm{D}} \int_0^{L/L_{\mathrm{D}}} \mathrm{e}^{((t^2/2)-d't)}\,\mathrm{d}t \\ &= L_{\mathrm{D}} I. \end{aligned} \tag{21}$$

The integral I depends on the following constants: k, q, L and ε, and the parameters T, N_{D} and $(V_c + V_{\mathrm{bi}})$. This integral has been evaluated by using the Maple code for T ranging from 200 to 400 K, N_{D} from 10^7 to $10^{12}\,\mathrm{cm}^{-3}$ (nominal values for CZT are in the order of $10^{10}\,\mathrm{cm}^{-3}$) and assuming a relative permittivity of 10. Numerical results computed for values of V_c over the range of interest perfectly fit to the expression L_{D}/d (see Fig. 2). In these calculations, V_c was assumed to be much larger than V_{bi}. Therefore, Eq. (12) can be re-written as

$$j = qD_n N_{\mathrm{c}}\,\mathrm{e}^{-(q/kT)\phi_{\mathrm{B}n}}\left[1 - \mathrm{e}^{-(q/kT)|V_c|}\right]\frac{d}{L_{\mathrm{D}}^2} \tag{22}$$

where $|V_c|$ was used for the absolute value of the voltage. In a detailed expression,

$$\begin{aligned} j &= qD_n N_{\mathrm{c}}\,\mathrm{e}^{-(q/kT)\phi_{\mathrm{B}n}}\left[1 - \mathrm{e}^{-(q/kT)|V_c|}\right] \\ &\quad \times \frac{qN_{\mathrm{D}}}{\varepsilon}\frac{q}{kT}\left[\frac{\varepsilon}{qN_{\mathrm{D}}L}(|V_c| + V_{\mathrm{bi}}) + \frac{L}{2}\right] \\ &= \frac{q^2}{\varepsilon}\mu_n N_{\mathrm{c}} N_{\mathrm{D}}\left[\frac{\varepsilon}{qN_{\mathrm{D}}L}(|V_c| + V_{\mathrm{bi}}) + \frac{L}{2}\right] \\ &\quad \times (1 - \mathrm{e}^{-(q/kT)|V_c|})\,\mathrm{e}^{-(q/kT)\phi_{\mathrm{B}n}}. \end{aligned} \tag{23}$$

From Eq. (23) it can be seen that the dependence of j with V_c in the diffusion model is

$$j = (\alpha + \beta|V_c|)(1 - \mathrm{e}^{-(q/kT)|V_c|}). \tag{24}$$

Regarding the dependence of j with T, the following considerations are taken into account:

- For the values of interest for $|V_c|$ in this work:
  - According to the position of Fermi level in the CdZnTe band gap, qV_{bi} is expected to be very low (Bolotnikov et al. [11] use the value 0.03 eV for this parameter). In this work, $|V_c|$ will always be much larger than V_{bi}.
  - In the expression in the square brackets of Eq. (23), the term $\varepsilon/(qN_{\mathrm{D}}L)(|V_c| + V_{\mathrm{bi}})$ is

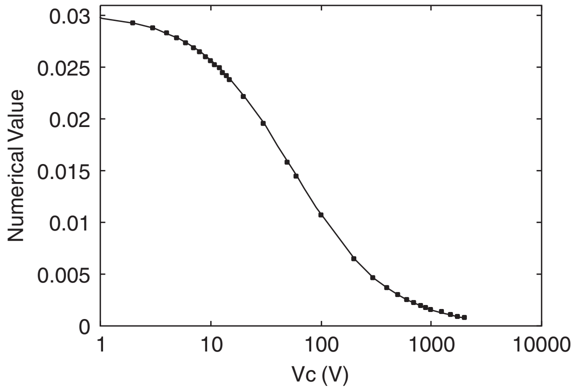

Fig. 2. Comparison of a set of single values computed for the integral I (filled dots) with L_D/d (line) in the whole range of $|V_c|$.

dominant over $L/2$ in most of the cases. Thus, the dependence of j with N_D is not critical, since its presence in the denominator of this expression is compensated by the dependence with N_D of the numerator.

- The dependence of N_c with T is as $T^{3/2}$, as shown below.
- The dependence of the mobility with T is not clear. It is known to decrease as T^{-x}, with x generally between 0.5 and 1. In this paper, a dependence with $T^{-0.5}$ is accepted. Experimental arguments supporting this assumption are provided in Ref. [5].
- For the values of $|V_c|$, the quantity $e^{-(q/kT)|V_c|}$ decreases rapidly to zero. Thus, the term $1 - e^{-(q/kT)|V_c|}$ is not affected significantly with T.

In line with the above assumptions, the dependence of j with T will be considered to be

$$j = \lambda T e^{-(q/kT)\phi_{Bn}}. \qquad (25)$$

The diffusion theory was used to model the detector's electrical response by fitting experimental results to the theoretical calculations provided by the developed formulation. $\phi_{Bn}(V)$ and N_D (cm^{-3}) are left as parameters to be evaluated from the fit. Regarding the other parameters in Eq. (23), the following values and expressions are considered:

- $\varepsilon = 10\varepsilon_0$.
- $N_c = 2(2\pi m^* kT/h^2)^{3/2}$, where h is the Plank's constant and m^* is the electron effective mass. A value of $m^* = 0.11 m_0$, in units of the free electron mass, is used in this work. This value is the one accepted for CdTe (being $m^* = 0.15 m_0$ for ZnTe) [13].
- The parameter μ_n is assumed to be $900\,cm^2/(Vs)$ at room temperature. As mentioned above, this parameter was also assumed to vary with temperature as $T^{-0.5}$.
- Since $|V_c| \gg V_{bi}$, the influence of this parameter in the fit of experimental values to Eq. (23) is not relevant and was disregarded. This simplification was shown to be valid in the two areas studied in the detector. The parameters obtained in the fit of the experimental data to the diffusion model were found to be unaffected by this parameter.

3. Experimental results

3.1. Experimental setup

The $I-V$ curves reported in this paper were acquired by making use of a Keithley electrometer, model 6514. Two programmable voltage sources were used: a Bertan 230-03 high-voltage power supply, in the range ± 50 to $\pm 2000\,V$ and the voltage source of an ADVANTEST electrometer model TR8652 in the range 0 to $\pm 20\,V$. The detector was housed in an electromagnetic shielding box and connected to the electrometer and power supplies through a triaxial connection. The detector box was located in a climatic chamber DYCOMETAL Dl-100. A PT-100 temperature sensor was installed in the detector box to control the temperature during the current measurements. The setup was completed by surrounding the detector box with external material to increase the thermal stability of the sensor.

Two regions of the detectors were studied: the bulk and the anode surface. In the bulk, the current flowing from the cathode to the two coplanar anodes was measured. The cathode was connected to the voltage power supply and both anodes were connected in parallel to the electrometer input. For the measurements in the anode surface, one anode was connected to the power supply and the other to the electrometer. The cathode was set to ground. In both of the units tested, the anode grid was surrounded by a guard ring (a viewgraph of the anode-guard-ring pattern of these detectors can be seen in Refs. [4,5]). In all, the reported measurements, the guard ring was connected to ground, as it would be during the normal operation of the detector. In this way, the leakage current in the lateral surfaces was avoided.

A program was developed specifically for these tests in order to automate the measurements. The code, which was built in LabWindows, controlled the voltage source and the electrometer, and logged the temperature of the sensor just after each current measurement. Each voltage–current curve was pre-programmed by selecting the two (upper and lower) voltage limits, the amplitude of the voltage step between consecutive measurements and the stabilization time on each step. Before starting a curve, the temperature was checked to make sure that it was sufficiently stable in the sensor. Deviations from the fixed temperature lower than $\pm 0.1\,^{\circ}\mathrm{C}$ were registered in all the measurements reported in this paper.

In the measurements at the high-voltage range (± 50 to ± 2000 V), a stabilization time of 2 min was selected before moving toward the next voltage value in steps of 50 V. In the low-voltage range (0 to ± 20 V), the bias step was 50 mV and the stabilization time 4 s. The evolution of the current during the stabilization time was checked in detail beforehand, in order to confirm the reproducibility of the current values. As a matter of fact, the evolution of the current against time was significantly dependent on the sensor temperature. For an example, Fig. 3 shows the relative values of the current in the bulk during the stabilization time for different temperatures. In order to compare the stabilization process at different temperatures, the values shown in Fig. 3 were normalized, setting to 1.0 the values at a time sufficiently large to be considered as stable. For each temperature, $t = 0$, the origin in the time axis, corresponds to the time when the bias was raised from the last voltage position. Fig. 3 confirms that the current reached its asymptotic limit in all the temperatures within the selected stabilization time.

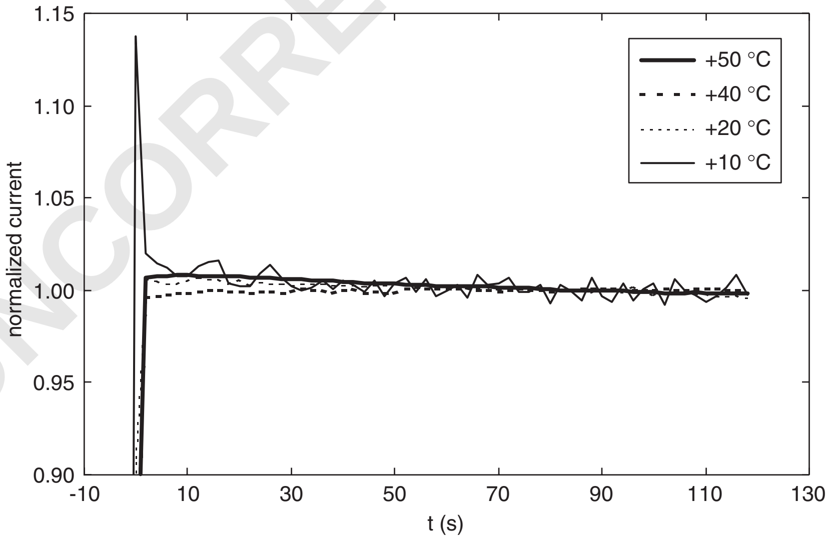

Fig. 3. Evolution of the current in the bulk during the stabilization time for different temperatures. Presented data were normalized to the final reached values at each corresponding temperature.

3.2. Cathode–anode region

A representative example of the experimental data collected in this region for the detector M02.2-1 is presented in Fig. 4. This corresponds to the positive branch of the $I-V$ curve collected at room temperature. The nominal operation bias for this detector is between 1000 and 2000 V. In this work, attention was paid to the curve at voltage values larger than 500 V. The trends of the currents below this bias were of second interest to us. In line with the comments above, linear–linear or log–linear representations are the best options to give details in the high-voltage region. Figs. 4a and b present the same results in linear and logarithmic Y-axis. These figures compare the experimental results obtained at room temperature with those obtained with the diffusion model. It can be seen that the diffusion model accurately fits the experimental data for $V > 500$ V. For the case shown in this figure, the diffusion model is sufficiently accurate and there is no need to use more complex models, such as ITD. Nonetheless, it must be pointed out that this model fails below 100 V, as the log–log plot shows. In Fig. 4c, the results shown in Figs. 4a and b are re-scaled again. The diffusion model overestimates the current density at low voltages. For this low-voltage range, the ITD model will provide a better approach. As previously mentioned in Section 2.1, the presence of an interfacial layer significantly reduces the current at low biases.

The bulk region was studied for the detector M02.2-1 in the temperature range -20 to $+60\,^{\circ}$C. Over this entire range, the curves exhibited rigorous linear trends for $|V_c| > 100$ V. Positive and negative branches showed a perfect symmetry. The results are presented in Fig. 5. For each experimental curve, the evaluations with the diffusion model at the corresponding temperatures are presented. The values obtained for ϕ_{Bn} from the least-squares fit to the diffusion Eq. (23) are given in Table 1. The order of magnitude found in the fit for N_D is $\sim 10^8\,\mathrm{cm}^{-3}$. The fitting procedure cannot provide a more precise value for this parameter. Table 1 shows that the values found for ϕ_{Bn} are very uniform in the temperatures studied. Fig. 5 confirms that the diffusion model, although simple, is sufficiently accurate to understand the current trends of detector M02.2-1 in the cathode–anode region. Attention must be paid to the lowest temperatures, where the fit is less precise than at room and high temperatures.

Results in this region for the detector M0904 are shown in Fig. 6 and Table 2, for the negative branches of the $I-V$ experimental curves at six different temperatures. Previous comments for detector M02.2-1 are confirmed. In this case, the variations of ϕ_{Bn} with T are slightly more evident. The current density found for the two detectors, taking into account the differences in the effective area of their electrodes, are similar.

The physical interpretation of the results presented in this section can be given by making use of the models presented in Section 2.1. In the ITD model, the parameter θ_n gives the fraction of electrons passing through the interfacial layer ($\theta_n = 1.0$ means complete absence of insulating layer) [12]. On the other hand, the voltage drop across the interfacial layer leads to an exponential rise of the saturation current. We have not observed this exponential rise, at least in our range of interest, which means that the potential barrier lowering is not significant. Furthermore, the estimated values for θ_n in the fit of experimental data with the ITD formulation were in most cases close to 1. According to these two results, we should expect that the theoretical curves calculated for the experimental data by making use of the ITD model would follow the diffusion-limited case, the so-called "D" curves in Ref. [12]. The diffusion model presented in this paper is just a simplified version of the ITD model, easier to implement in our simulations but fully compatible with previous works. As it is known [14], in the diffusion limit the electrons in the cathode are in equilibrium with the metal and the free carrier concentration at the cathode remains independent of the applied voltage at moderate values of bias. The saturation current in this case is proportional to the carrier concentration and electric field at the cathode.

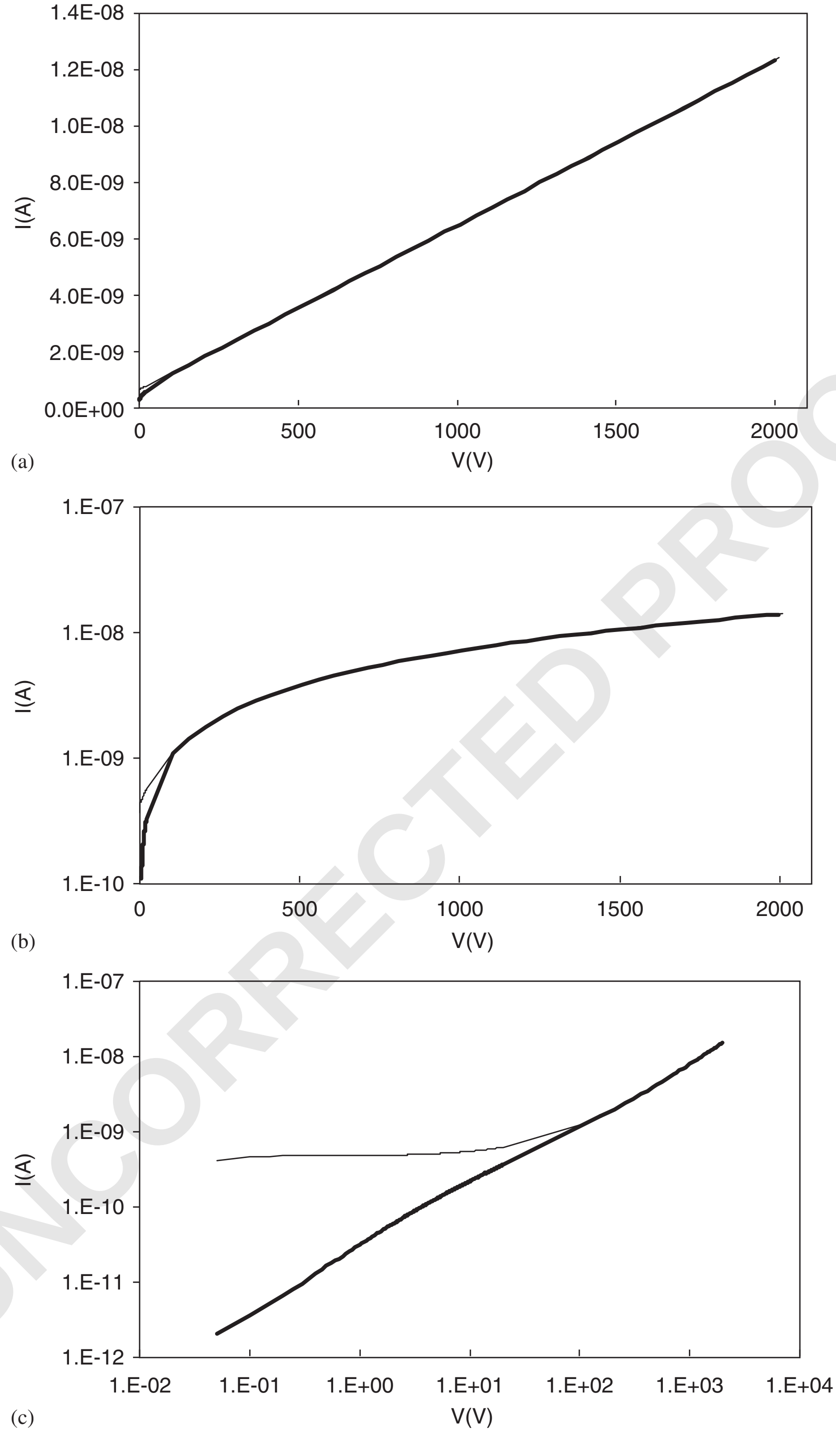

Fig. 4. $I-V$ curve collected in the cathode–anodes region for detector M02.2-1 at $T=21\,^{\circ}\mathrm{C}$ (solid line), together with the values provided by the diffusion model in this range (thin line): (a) linear–linear scale; (b) log–linear scale and (c) log–log scale.

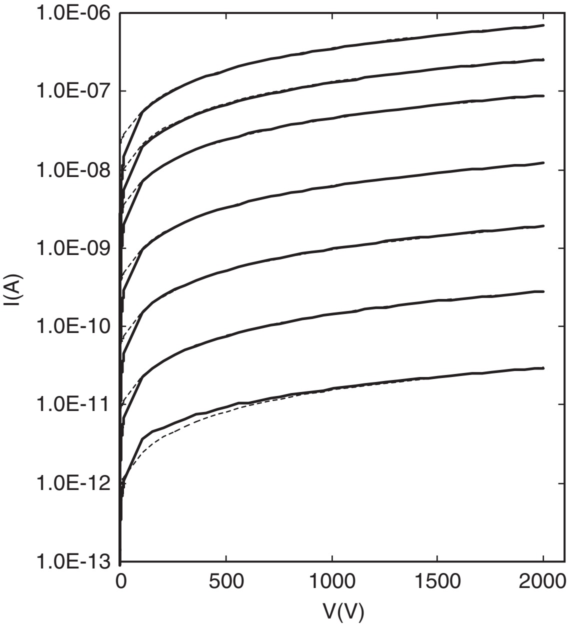

Fig. 5. $I - V$ curves collected in the cathode–anodes region of the detector M02.2-1 at the temperatures −21.9, −7.5, −6.1, 20.8, 38.6, 48.9 and 59.2 °C (thick lines). The fits to experimental data provided by the diffusion model are shown for each temperature (thin dashed lines).

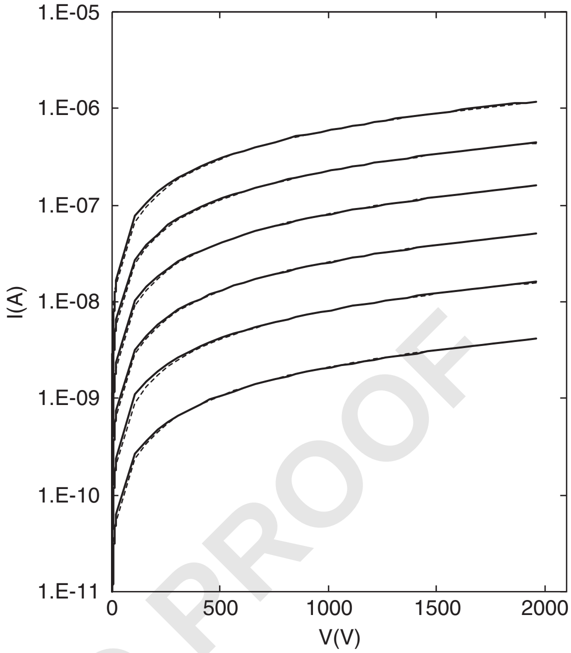

Fig. 6. $I - V$ curves collected in the cathode–anodes region of the detector M0904 at the temperatures 8.8, 19.3, 29.5, 39.9, 49.7 and 59.6 °C (thick lines). The fits to experimental data provided by the diffusion model are shown for each temperature (thin dashed lines).

Table 1
Barrier height values calculated by the diffusion model for detector M02.2-1

T (°C)	ϕ_{Bn} (V)
−21.9	0.871
−7.5	0.871
6.1	0.871
20.8	0.871
38.6	0.872
48.9	0.872
59.2	0.873

Table 2
Barrier height values calculated by the diffusion model for detector M0904

T (°C)	ϕ_{Bn} (V)
8.8	0.785
19.3	0.781
29.5	0.779
39.9	0.776
49.7	0.772
59.6	0.769

3.3. Anode surface

The anode surface in a coplanar detector is a critical region. The coplanar electrodes are constituted by two arrays of strips inter-digitally located in this surface. The gap between strips is very narrow, and the effective total length of each anode is very long. Therefore, this area is expected to show high leakage currents. The leakage currents negatively affect the electronic noise inherent to the detector. Furthermore, the coplanar technique [15] is not efficient in a device with high conductivity between strips. As a consequence, a lot of effort was made in the treatment of this surface to minimize the leakage current.

Fig. 7 shows a representative current–voltage response of this region for the detector M02.2-1.

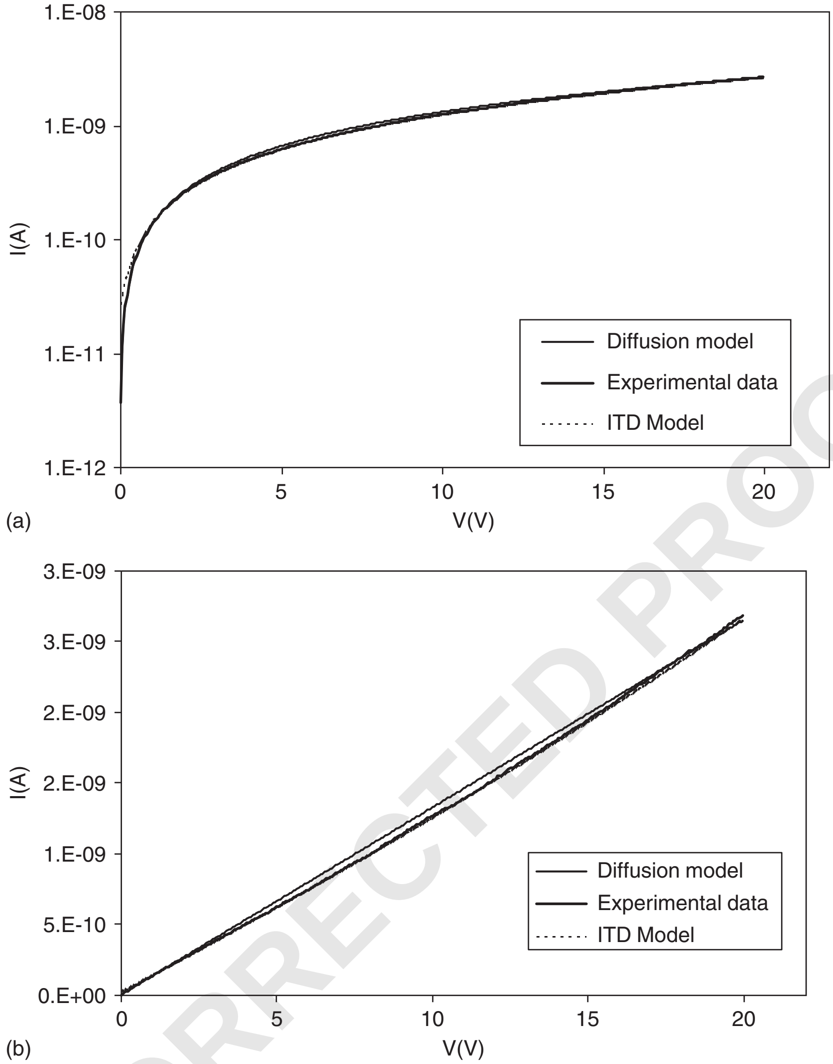

Fig. 7. $I-V$ curve collected in the anode surface of detector M02.2-1 at $T = 19.3\,°C$, together with values provided by the ITD and diffusion models in this range: (a) log–linear scale and (b) linear–linear scale.

These data were acquired at room temperature. Although the curve in the log–linear scale shows a correct trend of the diffusion model (Fig. 7a), the same plot in a linear scale (Fig. 7b) reveals that the linearity expected by the diffusion theory is not strictly followed by the experimental data. Independently of the behavior of the $I-V$ curve at low voltages, the ITD model seems to be a better approach for this region in the operation voltage range of interest, i.e., above 10 V. Regarding the ITD model, caution must be paid when interpreting the results. This model depends on a minimum of four fitting parameters. An acceptable fit to a function with four degrees of freedom is easy to reach, but this fit can lead to non-accurate or wrong physical interpretations of the results.

The results in Fig. 7 for detector M02.2-1 are confirmed in Fig. 8, in the range of temperatures reported in Table 3. The diffusion model is not sufficiently accurate to fit the two lower tempera-

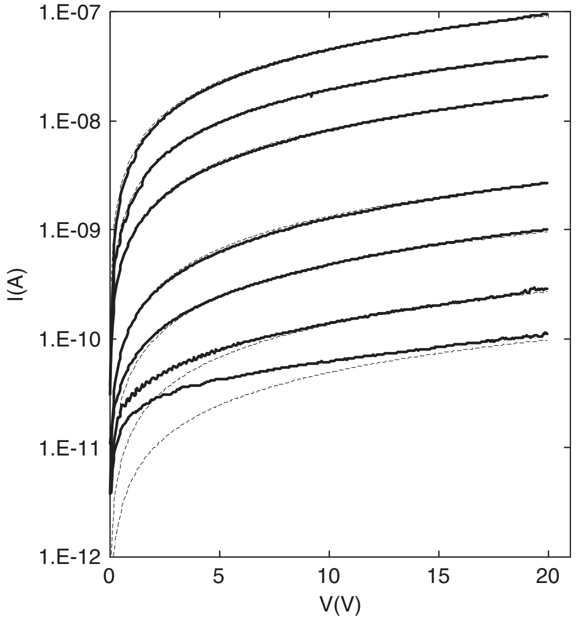

Fig. 8. $I-V$ curves collected in the anode surface of detector M02.2-1 at the temperatures −18.1, −4.9, 6.6, 19.3, 38.8, 49.3 and 58.7 °C (thick lines). The fits to experimental data provided by the diffusion model are shown for each temperature (thin lines).

Table 3
Parameters given by the diffusion and ITD models to data in Fig. 8 for the detector M02.2-1

T (°C)	Diffusion model	ITD model	
	ϕ_{Bn} (V)	ϕ_{Bn} (V)	θ_n
−18.1	0.720	0.693	0.013
−4.9	0.735	0.737	0.100
6.6	0.737	0.739	0.200
19.3	0.746	0.749	0.290
38.8	0.748	0.750	0.600
49.3	0.751	0.752	0.600
58.7	0.749	0.746	0.062

tures, although it provides a good approach for the higher temperatures. The values obtained with the two models for the most relevant parameters in their corresponding formulations are given in Table 3. In this table, we show the fitted values obtained for ϕ_{Bn} in the diffusion model and the fitted values obtained for ϕ_{Bn} and θ_n in the ITD model. As in the bulk region, the order of magnitude found for N_D was $\sim 10^8\,cm^{-3}$. Experimental $I-V$ curves acquired for the detector M0904 are shown in Fig. 9, together with the fit to the diffusion model. The values obtained for the parameters in the fits to the diffusion and ITD formulations are given in Table 4. In this detector, only temperatures above 0 °C were considered.

In line with the values presented in Tables 3 and 4 for the diffusion model, the following observations can be made:

(1) Variation of ϕ_{Bn} with T is more significant in the anode surface than in the bulk for detector M02.2-1. The opposite result was found for the detector M0409. Although the variation of ϕ_{Bn} with T in Table 3 could be considered as negligible at the beginning, its dependence on the current estimate is very significant.
(2) According to the effective areas of the anode regions in the two detectors, the current density in the anode surface of detector M0904 is significantly larger, nearly five times, than in the same region of detector M02.2-1. This result was confirmed at several temperatures.
(3) The barrier height in the anode surface is lower than in the bulk.

The conclusion reached from the results presented for the anode surface of the two detectors is that the diffusion model is a valid approach at the temperature and bias currently used during typical detector operation, but this theory is too simplistic to model the device in the whole range. Contradictory results are obtained from the data shown for the ITD model in Tables 3 and 4. If we observe the values calculated for the parameter θ_n, it can be seen that, according to the interpretation provided in Refs. [12,14] for this parameter, $I-V$ curves presented in Figs. 8 and 9 should be closer to the thermionic-limited case than to the diffusion-limited case. This is an erroneous conclusion, since the diffusion model has been demonstrated to be an acceptable approach. According to Figs. 8 and 9, values of θ_n close to one were expected. Since this is not the case, we assume that the ITD formulation does not provide a consistent inter-

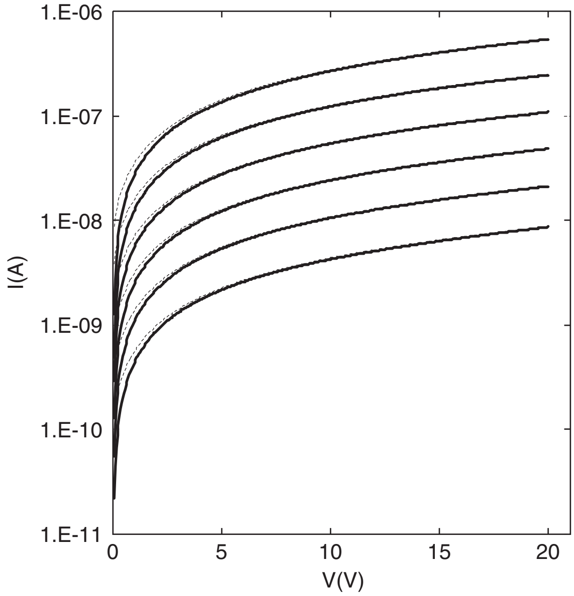

Fig. 9. $I-V$ curves collected in the anode surface for detector M0904 at the temperatures 9.76, 19.4, 29.2, 39.2, 49.4 and 59.5 °C (thick lines). The fits to experimental data provided by the diffusion model are shown for each temperature (thin lines).

Table 4
Parameters given by the diffusion and ITD models to data in Fig. 9 for the detector M0904

T (°C)	Diffusion model	ITD model	
	ϕ_{Bn} (V)	ϕ_{Bn} (V)	θ_n
9.76	0.697	0.690	0.049
19.4	0.698	0.693	0.057
29.2	0.701	0.696	0.069
39.2	0.703	0.701	0.097
49.4	0.705	0.703	0.118
59.5	0.705	0.704	0.131

pretation of the results obtained in this region. This is compatible with some conclusions previously reported [12,14]. The anode surface leakage current is not dominated by the current in the bulk, because if this were the case, it should follow the ITD approach, as demonstrated in the previous section. Therefore, we can think that the anode current is mainly due to the detector surface, in which the presence of a low-resistivity surface layer with different chemical structures than the bulk has been previously reported. This layer is supposed to be created during the electrode deposition. In this process, an excess of fixed charge is created in the first atomic layers of the semiconductor. The resistivity in the two studied regions was estimated for our detectors, according to Ohm's law, in the linear region of the $I-V$ curve at low voltages ($V<2$ V). For the M02.2-1 unit, the bulk resistivity at room temperature was $1\times10^{10}\,\Omega$ cm. The surface resistivity between the anode grids was $1\times10^{12}\,\Omega$. The resistivity in this area is the surface resistivity times the surface thickness. It is difficult to estimate this thickness. Other authors have estimated this thickness to be in the order of 0.1 μm [12]. Using the conservative (large) value of 1 μm, the resistivity in the anode surface region is two times lower than in the bulk.

According to Ref. [14], the conducting layer on the detector anode surfaces can be considered as a metal–semiconductor–metal system, with properties differentiated from the bulk. In our case, this metal–semiconductor–metal system follows the diffusion model, with the limitations reported above. A second model applied in the literature for this surface is the space-charge-limited current (SCLC) theory [14]. In this interpretation, the space charge accumulated in this conductive layer limits the current between anodes. The simplified SCLC theory for single injection is based on three assumptions [16]:

(1) Carrier mobility is supposed to be constant in the considered electric field range.
(2) Diffusion currents are neglected.
(3) The cathode is taken to be an infinite reservoir of electrons available for injection.

The first approximation is valid for field strengths that are not too high. The working biases in our devices always lead to electric fields compatible with this assumption. The second one simplifies the theory and makes it mathematically tractable to elementary analysis. The third approximation comes from an ideal injecting contact. Under this ideal regime, the theory is independent of the contact and makes it a universal theory. Actually, this ideal regime is a strong simplification of the reality and thus this theory is conceptually elemental compared with the one presented in Section 2. The last two approximations are closely related, since an infinite concentration of electrons necessarily gives an infinite diffusion current at the contact. This means that the simplified theory built on two and three is necessarily wrong in the immediate vicinity of the injecting contact, but gives good descriptions of the current flow over the bulk and of the device current–voltage characteristics. This is generally correct, even for devices much thinner than the ones considered in this work.

In this formulation, the interesting features of the $I-V$ curves are confined within three limiting curves [17]: Ohm's law ($J \propto V$), Child's law ($J \propto V^2$) and the trap-filled-limit curve ($J \propto V^{\alpha}$, with $\alpha \gg 2$). The simplest possible situation is a perfect insulator (or semiconductor) free of traps and with a small concentration of free carriers in thermal equilibrium. In this case (i), the injected carrier concentrations are much higher than the thermal free carrier one. In a second case (ii), the semiconductor is free of traps and the thermal free carriers are the majority, with the injected charge negligible. In the case (i), the current density J is proportional to V^2; in the case (ii), $J \propto V$. The presence of traps in the forbidden gap of the semiconductor will lead to different power-law dependencies of J with V, depending on the distribution and type of traps, but limited in any case by the trap-filled-limit curve.

We will demonstrate hereafter that the detectors presented in this paper can be understood through case (ii), the so-called Ohmic regime in the SCLC theory.

In the Ohmic regime, the thermally generated carrier density n_0 will be much higher than the injected carrier density, so $n(x) \cong n_0$, where $n(x)$ is the actual spatially varying free electron concentration. Thus, the carrier concentration that contributes to the current flow will be n_0, but the net carrier concentration in the space charge is nearly zero, since the net contribution in Poisson equation is $n(x)-n_0$. Thus,

$$j = \mathrm{e}\,\mu n_0 E_{\Omega} = ct\,\mathrm{e}. \tag{26}$$

Eq. (26) is just the current flow Eq. (1) in the absence of diffusion. In this regime,

$$j = \frac{\mathrm{e}\mu n_0}{L} V_c. \tag{27}$$

This simple equation has been used to model the experimental data presented in Figs. 8 and 9. The thermally generated free carrier concentration has been calculated from its dependence with N_c, similarly as in Eqs. (9) and (10). Results are presented in Figs. 10 and 11 for detectors M02.2-1 and M0904, respectively. Very similar results to those provided by the diffusion model are obtained for detector M02.2-1. Slightly better approach was obtained for detector M0904. Again, bad results are found at temperatures below zero.

The fact that the $I-V$ curves in the anode region do not show a transition voltage from Ohmic law to Child's law and that no evidence in the curves were found of traps, in the operation temperature and bias ranges, are indications of the quality of the surface treatment and electrode deposition.

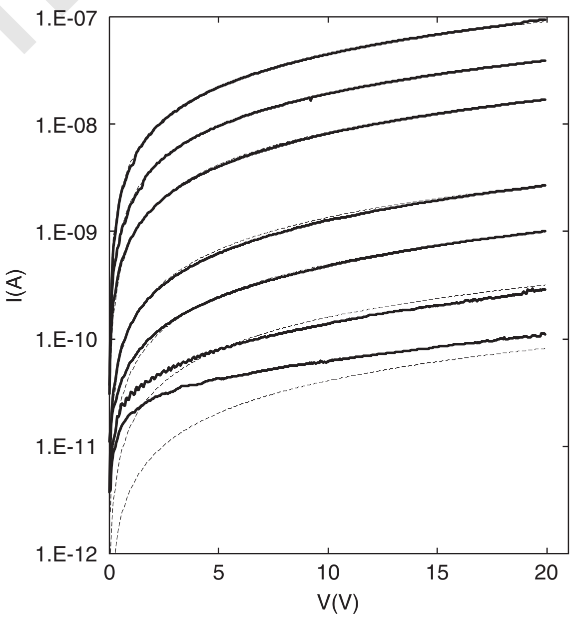

Fig. 10. The experimental results shown in Fig. 8 at the temperatures −18.1, −4.9, 6.6, 19.3, 38.8, 49.3 and 58.7 °C (thick lines), compared with the fit provided by the SCLC formulation for each temperature (thin lines).

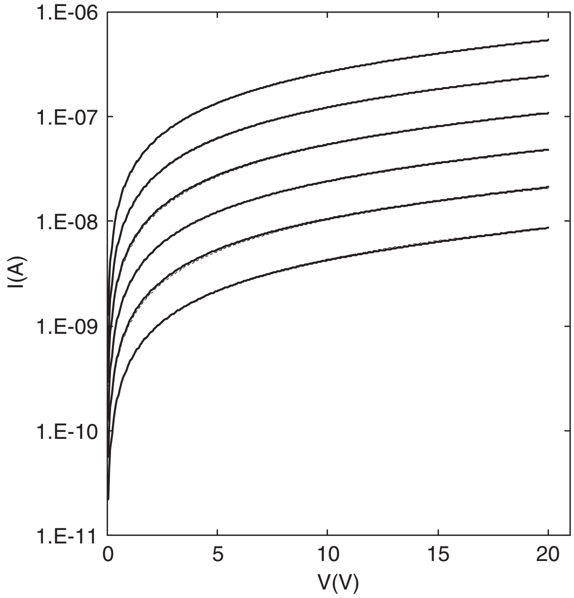

Fig. 11. The experimental results shown in Fig. 9 at the temperatures 9.76, 19.4, 29.2, 39.2, 49.4 and 59.5 °C (thick lines), compared with the fit provided by the SCLC formulation for each temperature (thin lines).

4. Implications for future designs

The presence of the conductive layer in the anode region is known to influence the collection by the anodes of the charge produced by the radiation in the bulk [18]. The expected optimum differential bias between anodes in the detector can be altered by this effect. A digital study of the collection efficiency was performed at operation bias. The detector M0904 was biased at $-1200\,\mathrm{V}$ at the cathode. A differential voltage of $30\,\mathrm{V}$ between anodes was used. The digitization system described in Ref. [5] was used to acquire and process pulses induced by radiation generated directly by the preamplifiers A250 connected to the two anodes and the cathode. The central region of the detector was exposed to flood irradiations with a ^{90}Sr beta source with the areas closer to the guard ring being collimated. A collection of pulses was acquired and their shapes analyzed. Those revealing severe or significant non-uniform trapping throughout the charge path within the bulk were rejected. In the cases analyzed, the total charge was collected by the collecting anode. There were no traces of charge sharing between anodes, i.e., in no cases non-collecting anode presented final amplitude larger than zero. The conclusion of this study was that at these cathode and differential anode biases the detector is fully efficient. All the charges generated by the radiation were collected by the collecting anode.

A bulk with constant resistivity was assumed for the design of the coplanar anodes in the detectors presented in this paper. Electrical potential and field distributions in the detectors were studied, assuming the electrostatic approach, by making use of codes such as Coulomb or ANSYS. Once an anode design was found with weighting potentials sufficiently balanced, the design was validated by studying the charge collection efficiency. Charge collection in collecting and non-collecting anodes was addressed, for acceptable values of differential anode and cathode bias. If the minimum differential voltage for the collecting anode to be fully efficient is too large, large leakage currents between anodes, and undesired high electronic noise, must be expected in the detector.

In the particular case of detector M02.2-1, the electric field within this detector at the bias conditions reported above and a value for the bulk resistivity of $10^{10}\,\Omega\,\mathrm{cm}$ was modeled with ANSYS 6.0. The charge drift within the bulk was simulated by moving a point distribution of charges with a mobility equal to $1000\,\mathrm{cm}^2/(\mathrm{Vs})$ and assuming a trapping time sufficiently large for the charge to reach the anode surface without important degradation. The diffusion process was disregarded. The results were calculated for charge originated at different positions in the cathode side ($z = -10\,\mathrm{mm}$), its x coordinates distributed from a position just below the center of a strip of the non-collecting anode to the center of the consecutive strip (in the collecting anode). A 2D model of the detector was used, i.e., assuming the layer $y = 0$ and supposing the detector to be infinite in this dimension. Fig. 12 shows the charge drift in the region close to anode surface for the trajectories being studied. The tracks were almost perfectly straight from $z = -10$ to $-1\,\mathrm{mm}$. It can be seen that a significant proportion of charge originated

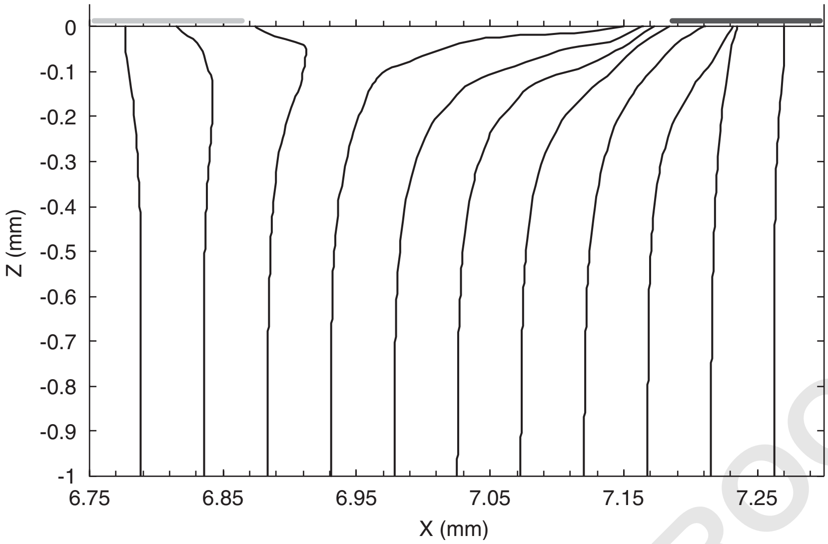

Fig. 12. Trajectories of electrons generated in the cathode surface, drifted by a 2D electric field toward anode surface. The x coordinates at starting points were distributed from a position just below the center of a strip of the non-collecting anode (represented in gray in the plot) to the center of the consecutive strip in the collecting anode (represented in black). The electric field was simulated by ANSYS for the electrode pattern in detector M0904 and a bulk resistivity of $1.0 \times 10^{10}\,\Omega\,\mathrm{cm}$. Cathode bias: -1200 V; non-collecting anode bias: 0 V; collecting anode bias: $+30$ V. Only the region near the anode side is shown.

in positions of the gap between anodes does not reach the collecting anode. The inclusion of the diffusion process in this track would not fully compensate for this effect.

If a layer with lower resistivity in the anode face is included in the ANSYS model, the results would largely be different. See Fig. 13, where a conductive layer 20 μm thick and resistivity two order of magnitude lower than the rest of the bulk is considered. This simulation can only provide qualitative interpretations, because the conductive layer is much thicker than that expected in the real detector. This value for the layer thickness was imposed by implementation constraints in the ANSYS model. Besides, the paths presented in Fig. 13 are not exactly as expected, since some of them would lead to induced charge waveforms with profiles not found in the laboratory. Nonetheless, in spite of the above limitations, this simulation is valid to identify the effects of the low-resistivity layer identified in the detectors from their $I-V$ currents. It is obvious that this layer must be considered in future designs for a better approach on the charge collection efficiency estimate.

5. Discussion

The interfacial-layer theory developed for the metal–semiconductor Schottky barrier was confirmed to be valid for the bulk of large volume CdZnTe detectors presented in this paper. The diffusion limit, a less general and more simple approach, was demonstrated to be sufficiently accurate for modeling the cathode–anode electric performance of the devices in the operation range. These detectors have been designed to work at temperatures between $+10$ and $+50\,^{\circ}$C and biased to ~1000 V in the cathode. In these ranges, the diffusion model acceptably fits experimental results. The validation of the diffusion limit of the theory enables us to significantly simplify the electrical model of the bulk in our devices. In detector M02.2-1, the diffusion model is not accurate at lower biases. In this range, the presence

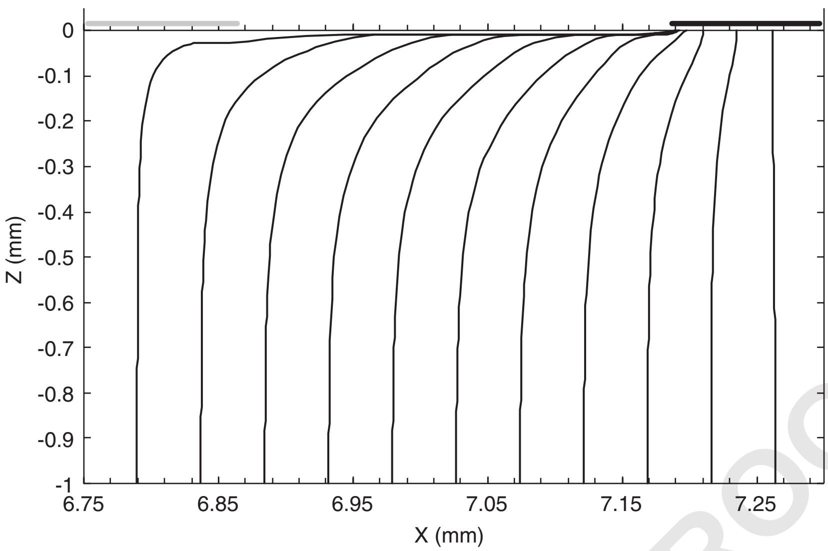

Fig. 13. Diagram of trajectories comparable to the one displayed in Fig. 12. In this case, the electric field was simulated for a detector with bulk resistivity of $10^{10}\,\Omega$cm and a 20 μm thick layer in the anode face with resistivity two order of magnitude lower than the rest of the bulk. Biases were kept identical as those used in Fig. 12.

of the interfacial layer predicted by the ITD model is significant, and the inclusion of it would make the theoretical current values smaller at low biases.

In the anode face, the diffusion formulation is also valid to model our devices, but only in the operation temperature and bias ranges. It fails at lower biases and temperatures below zero. The ITD model fits our experimental results, but leads to contradictory conclusions, which confirms that the electrical properties of the surface and the bulk are rather different. Assuming the presence of a conductive layer reported by other authors and that the major contribution to the surface current is due to this layer, two models were compared for the interpretation of the $I-V$ experimental curves: the diffusion model and the SCLC theory. Both models leads to practically identical results for detector M02.2-1, but the SCLC model is more accurate for detector M0904. According to this result, it can be said that the surface treatment and electrode deposition in detector M0904 is of excellent quality: there is no significant presence of traps and the surface currents do not leave the Ohmic regime in the bias range of interest. But even in this favorable case, the concentration of space charge accumulated in the surface leads to a current much higher than the one in the bulk. Fortunately, electronic noise in the anode surface is less sensitive than expected to this current [19,20], because of well-known particular properties of space charge controlled currents [14]. The deviation of the detectors results from the models at lower temperatures and, in the case of detector M02.2-1, at low biases, cannot be explained within the frame presented in this work. This will be the base of future studies.

The effects of the conducting layer in the anode surface must be considered in future designs of coplanar, pixel or strip detectors. The influence of its presence on the estimate of charge collection efficiency was confirmed. From the conclusions reported in this work, a more realistic approach for the electric field profile in the detector can be considered in future works.

Acknowledgements

This work was supported by the Spanish Ministry of Education under Grant Ref.

TIC2002-02367. The authors thank Prof. Luis López-Bonilla, from The University Carlos III, Madrid, for his helpful suggestions on the theoretical modeling.

References

[1] J.M. Pérez, Z. He, D. Wehe, IEEE Trans. Nucl. Sci. NS48 (3) (2001) 272.
[2] J.M. Pérez, Z. He, D.K. Wehe, Y.F. Du, IEEE Trans. Nucl. Sci. NS49 (4) (2002) 2010.
[3] P.N. Luke, M. Amman, J.S. Lee, B.A. Ludewight, H. Yaver, Nucl. Instr. and Meth. A 458 (2001) 319.
[4] R. González, J.M. Pérez, Z. He, Nucl. Instr. and Meth. A 531 (2004) 544.
[5] R. González, J.M. Pérez, O. Vela, E. de Burgos, J.C. Oller, V. Gostilo, Spectrometric characterization of large volume CdZnTe coplanar detectors, IEEE Trans. Nucl. Sci., sent for publication.
[6] P.N. Luke, IEEE Trans. Nucl. Sci. NS42 (4) (1995) 207.
[7] S.M. Sze, Physics of Semiconductor Devices, second ed, Wiley, New York, 1981.
[8] G. Cisneros, P. Mark, Solid-State Electron. 18 (1975) 563.
[9] C.Y. Wu, J. Appl. Phys. 51 (7) (1980).
[10] C.Y. Wu, J. Appl. Phys. 53 (8) (1982).
[11] A. Bolotnikov, S.E. Boggs, C.M. Hubert Chen, W.R. Cook, F.A. Harrison, S.M. Schindler, Nucl. Instr. and Meth. A 482 (2002) 395.
[12] A. Bolotnikov, C.M. Hubert Chen, W.R. Cook, F.A. Harrison, I. Kuvvetli, S.M. Schindler, C.M. Stahle, B.H. Parker, Nucl. Instr. and Meth. A 510 (2003) 300.
[13] T.E. Schlesinger, J.E. Toney, H. Yoon, E.Y. Lee, B.A. Brunett, L. Franks, R.B. James, Mater. Sci. Eng. 32 (2001) 103.
[14] A.E. Bolotnikov, C.M. Hubert Chen, W.R. Cook, F.A. Harrison, I. Kuvvetli, S.M. Schindler, IEEE Trans. Nucl. Sci. NS49 (4) (2002) 1941.
[15] P.N. Luke, IEEE Trans. Nucl. Sci. NS42 (4) (1995) 207.
[16] M.A. Lampert, P. Mark, Current Injection in Solids, Academic Press, New York and London, 1970.
[17] M.A. Lampert, Phys. Rev. 103 (6) (1956) 1648.
[18] T.H. Prettyman, K.D. Ianakiev, S.A. Soldner, Cs. Szeles, Nucl. Instr. and Meth. A 476 (2002) 658.
[19] P.N. Luke, A. Amman, J.S. Lee, P.F. Manfredi, IEEE Trans. Nucl. Sci. NS48 (3) (2001) 282.
[20] P.N. Luke, A. Amman, J.S. Lee, IEEE Trans. Nucl. Sci. NS51 (3) (2004) 1199.